Geochimica et Cosmochimica Acta 414 (2026) 247–258

Contents lists available at ScienceDirect

Geochimica et Cosmochimica Acta

journal homepage: www.elsevier.com/locate/gca

Modeling of ^{231}Pa cycle and its implications on particle scavenging in the global ocean

Jing-Shan Meng, Wei-Lei Wang *

State Key Laboratory of Marine Environmental Science, College of Ocean and Earth Sciences, Xiamen University, Xiamen 361102, China

ARTICLE INFO

Associate editor: Franco Marcantonio

Keywords:
Protactinium-231
Reversible scavenging
Hydrothermal scavenging
Bottom scavenging
GEOTRACES
Data-constrained inverse model

ABSTRACT

Protactinium-231 (^{231}Pa) is a particle-reactive radionuclide whose distribution integrates the effects of scavenging and ocean transport, making it a powerful tracer of particle dynamics and a potentially useful tracer for ocean circulation. We present the first global ^{231}Pa inverse model that couples reversible scavenging by biogenic and lithogenic particles with two explicitly parameterized local sinks: bottom scavenging based on satellite-derived eddy kinetic energy (EKE) as a proxy for nepheloid-layer particles, and hydrothermal scavenging linked to ^{3}He flux as a proxy for hydrothermal particle inputs. Constrained by available ^{231}Pa observations, the model reproduces global dissolved ^{231}Pa distributions with a goodness-of-fit $R^2 = 0.79$, and quantifies the global removal budget: 71 % by biogenic particles, 24 % by bottom scavenging, and 4 % by hydrothermal scavenging. Sensitivity tests reveal that particulate organic carbon (POC) and particulate inorganic carbon (PIC) act as consistent net sinks throughout the water column, whereas biogenic silica (bSi) enhances deep-water ^{231}Pa through downward transport and release. Bottom scavenging strongly constrains deep-ocean ^{231}Pa, while hydrothermal scavenging is locally important near active ridges. This mechanistically informed, data-constrained framework advances our understanding of particle–tracer interactions and is directly transferable to other particle-reactive elements, with implications for biogeochemical modeling.

1. Introduction

Particle scavenging is a fundamental process that controls the spatial distribution of many trace elements in the ocean. In this process, sinking particles adsorb particle-reactive elements from the water column and transport them to the deep ocean and sediments (Goldberg, 1954; Anderson et al., 1983a; Anderson et al., 1983b). This classical top-down process is reversible, indicating that the decreasing concentration of scavenging particles with depth releases surface-sourced elements in the deep ocean. The efficacy of particle scavenging is primarily determined by sinking mass and the geochemical composition of sinking particles (Chase et al., 2003; Hayes et al., 2015b). Environments governed by high particle flux, such as the euphotic layer and ocean margins, are very effective sinks for particle-reactive elements. This reversible scavenging process is crucial for regulating the oceanic residence times of trace metals and radionuclides, thereby influencing their availability for biological processes or their utility as geochemical tracers (Weber et al., 2018; Roshan et al., 2020; Lanning et al., 2023). Although reversible scavenging is widely considered to govern the distribution of particle-reactive radionuclides, recent evidence suggests that it may not be strictly reversible for certain trace metals (Du et al., 2025).

Recognizing the critical role of particle scavenging in shaping the distributions of trace elements and radionuclides in the ocean, the GEOTRACES program has conducted extensive basin-wide surveys, providing full-depth, high-resolution measurements of particle-reactive radionuclides (e.g., ^{231}Pa, ^{230}Th, ^{10}Be) and micronutrients (e.g., Fe, Al, Mn, Cu). Among these tracers, ^{231}Pa is a sensitive indicator of scavenging dynamics due to its strong particle affinity and short residence time in seawater (~50–200 years), compared to its radioactive decay half-life of 32,760 years (Robert et al., 1969). In seawater, dissolved ^{231}Pa is produced *in-situ* from the decay of Uranium-235 (^{235}U), which is soluble and maintains a relatively constant concentration in oxygenated seawater (Ku et al., 1977; Henderson and Anderson, 2003). Once formed, dissolved ^{231}Pa is rapidly removed from the water column through adsorption onto sinking particles. In addition to scavenging, dissolved ^{231}Pa is also transported laterally and vertically by ocean circulation, which redistributes it across different depths and ocean basins. Theoretically, given its globally uniform production rate, its

* Corresponding author.
E-mail address: weilei.wang@xmu.edu.cn (W.-L. Wang).

https://doi.org/10.1016/j.gca.2025.11.046
Received 11 August 2025; Accepted 26 November 2025
Available online 29 November 2025
0016-7037/© 2025 The Author(s). Published by Elsevier Ltd. This is an open access article under the CC BY license (http://creativecommons.org/licenses/by/4.0/).

vertical distribution can be largely interpreted by reversible scavenging (Bacon & Anderson, 1982), resulting in a characteristic linear increase of dissolved ^{231}Pa with depth (Chase et al., 2003; Deng et al., 2018; Gdaniec et al., 2020; Pavia et al., 2020; Levier et al., 2023).

The deviation from the idealized linear scavenging model measured in the Equatorial and South Atlantic indicates that processes other than reversible scavenging, such as localized enhanced advection and particle scavenging can strongly influence ^{231}Pa distribution (Moran et al., 2001; Moran et al., 2002). Nonlinearity in ^{231}Pa profiles has been primarily attributed to the effect of physical circulation. For example, the injection of ^{231}Pa-depleted waters associated with overturning circulation can lead to nonlinear vertical profiles in the North Atlantic (Cochran et al., 1987). More recently, high-vertical resolution observations have further revealed these deviations of ^{231}Pa profiles near the hydrothermal ridges and benthic nepheloid layers where are characterized by elevated particle fluxes from multiple interior ocean sources (Hayes et al., 2013; Hayes et al., 2015a; Pavia et al., 2018; Ng et al., 2020). A recent study summarized that bottom scavenging and hydrothermal scavenging are believed to be responsible for such anomalies in the profiles of ^{230}Th (Costa et al., 2020), a stronger particle-reactive radionuclide whose oceanic cycle is very close to the ^{231}Pa (Anderson et al., 1983a; Anserson et al., 1983b; Chase et al., 2002). These two processes are thought to contribute significantly to the nonlinear profiles of ^{231}Pa observed in localized regions. Moreover, ocean circulation can propagate these signals to broader spatial scales.

Bottom scavenging primarily occurs within the benthic nepheloid layer, which is generated by strong near-seafloor currents (>20 cm/s) and is characterized by elevated concentrations of sediment-derived resuspended particles (Ewing and Thorndike, 1965; Biscaye and Eittreim, 1977). Particle concentrations within the nepheloid layer can be two orders of magnitude higher than concentrations measured at mid-ocean, leading to a pronounced deficit of dissolved ^{231}Pa and an increase in its particulate phase (Chen et al., 2021). Apart from bottom scavenging, hydrothermal scavenging is another key removal process that regulates the distribution of ^{231}Pa near the mid-ocean ridges. Hydrothermal-sourced particle injection causes enhanced burial rates of particle-reactive elements in the vent areas (Lund et al., 2019; Middleton et al., 2020). For example, a previous study has revealed that intense hydrothermal scavenging, driven by hydrothermal particles such as particulate manganese (pMn) and particulate iron (pFe) across the mid-ocean ridges and back-arc basins, leads to enhanced removal of dissolved ^{231}Pa within the hydrothermal plume of Southeast Pacific Ocean (Pavia et al., 2018).

Additionally, enhanced particle flux in the continental boundaries and spatial gradients in scavenging intensity, can generate the lateral advection and eddy diffusion that transport dissolved ^{231}Pa toward regions with intensified removal. This enhanced removal near ocean boundaries, termed boundary scavenging, reflects the preferential extraction of particle-reactive elements in margin settings where particle concentrations are high (Bacon, 1988). Although this effect is generally considered minor, given that deep ocean mixing timescales (~centuries) exceed the residence time of ^{231}Pa, its contribution in certain regions may not be negligible, finally reducing ^{231}Pa gradients between the ocean interior and boundary margins (German et al., 1993; German et al., 1997; Pavia et al., 2019).

Over the past decade, several three-dimensional global models have been developed to simulate the ^{231}Pa cycle in the ocean (Gu and Liu, 2017; Rempfer et al., 2017; Lerner et al., 2020; Sasaki et al., 2022; Pöppelmeier et al., 2023; Scheen et al., 2025). These models, often implemented in forward mode, have incorporated increasingly detailed representations of particle types and parameterizations of processes such as bottom scavenging. However, current models still struggle to reproduce the observed ^{231}Pa distributions, particularly in the mid and deep ocean, and it remains unclear how different types of particles control ^{231}Pa cycle in the water column.

In this study, we hypothesize that the spatial variability in the global distribution of ^{231}Pa is primarily governed by the combined effects of reversible, bottom, and hydrothermal scavenging, superimposed on the background of large-scale circulation. Based on this hypothesis, we developed a global-scale ^{231}Pa inverse model coupled with an ocean circulation inverse model (OCIM2; DeVries and Holzer, 2019). Compared to previous models, we first adopted an empirical relationship between satellite-based eddy kinetic energy (EKE) and nepheloid particle concentrations to parameterize bottom scavenging near the seafloor. We also incorporated hydrothermal-sourced ^{3}He flux as a proxy to parameterize hydrothermal particle scavenging of ^{231}Pa near mid-ocean ridges. Using dissolved ^{231}Pa observations as a constraint, we optimized key scavenging parameters and performed a suite of sensitivity experiments to disentangle the contributions of reversible, bottom, and hydrothermal scavenging to the global distribution of ^{231}Pa. Therefore, the major goal of this paper is to answer the following question: how reversible, bottom, and hydrothermal scavenging shape the distribution of ^{231}Pa?

2. Materials and methods

2.1. Observational Data

Observational concentrations of hydrographic data including dissolved inorganic phosphorous (DIP), dissolved silicic acid (DSi), dissolved organic carbon (DIC), and total alkalinity (ALK) were obtained from the Global Ocean Data Analysis Project website, the second version (GLODAPv2, Lauvset et al., 2021). Global dissolved ^{231}Pa observations were downloaded from the BCO-DMO website (https://www.bco-dmo.org/dataset/969309). This dataset excluded the measurements in the Arctic Ocean. The ^{231}Pa data used in this study were binned onto the OCIM2 grid, which has a horizontal resolution of $2^\circ \times 2^\circ$ and 24 vertical layers, with vertical resolution decreasing with depth. The spatial distribution of observational ^{231}Pa in OCIM2 grid and the number of data points in each vertical layer are presented in the Fig. 1. This dataset has a total of 1731 dissolved ^{231}Pa observations distributed across all major ocean basins.

2.2. Particle fields

2.2.1. Biogenic particles

We obtained global fields of biogenic particles (Fig. S2) including POC, PIC, and bSi from a data-constrained biogeochemical inverse model (Wang et al., 2019; Fu and Wang, 2022; Wang et al., 2023, Fig. S3), which simulates the cycling of phosphorus (P), carbon (C), and silicon (Si) and is physically driven by OCIM2 transport operator. Below, we briefly introduce how we modeled biogenic particle fields.

The global distributions of POC and PIC are obtained from Fu and Wang (2022), which simulates the coupled oceanic cycling of carbon and phosphorus. The sinking speeds of POC and PIC are implicitly built in a particle flux divergence operator (**PFD**) according to Kriest and Oschlies (2008). Specifically, the POC flux is modeled using a power-law function (a.k.a., the Martin curve):

$$F_{POC}(z) = F_{POC}(z_0)(z/z_0)^{-b_C} \quad (1)$$

where $F_{POC}(z_0)$ and $F_{POC}(z)$ are the POC flux at the euphotic depth z_0 (~73 m) and depth z, respectively. b_C controls the attenuation of POC flux with depth and is obtained from Fu and Wang (2022). PIC flux is modeled with an exponential function:

$$F_{PIC}(z) = F_{PIC}(z_0)\, e^{(z-z_0)/d_{PIC}} \quad (2)$$

where d_{PIC} is a characteristic length scale for PIC dissolution, also determined through model optimization. This formulation leads to a more gradual decrease in PIC flux with depth compared to the steeper attenuation observed for POC, consistent with observations that PIC is more resistant to dissolution in the upper ocean.

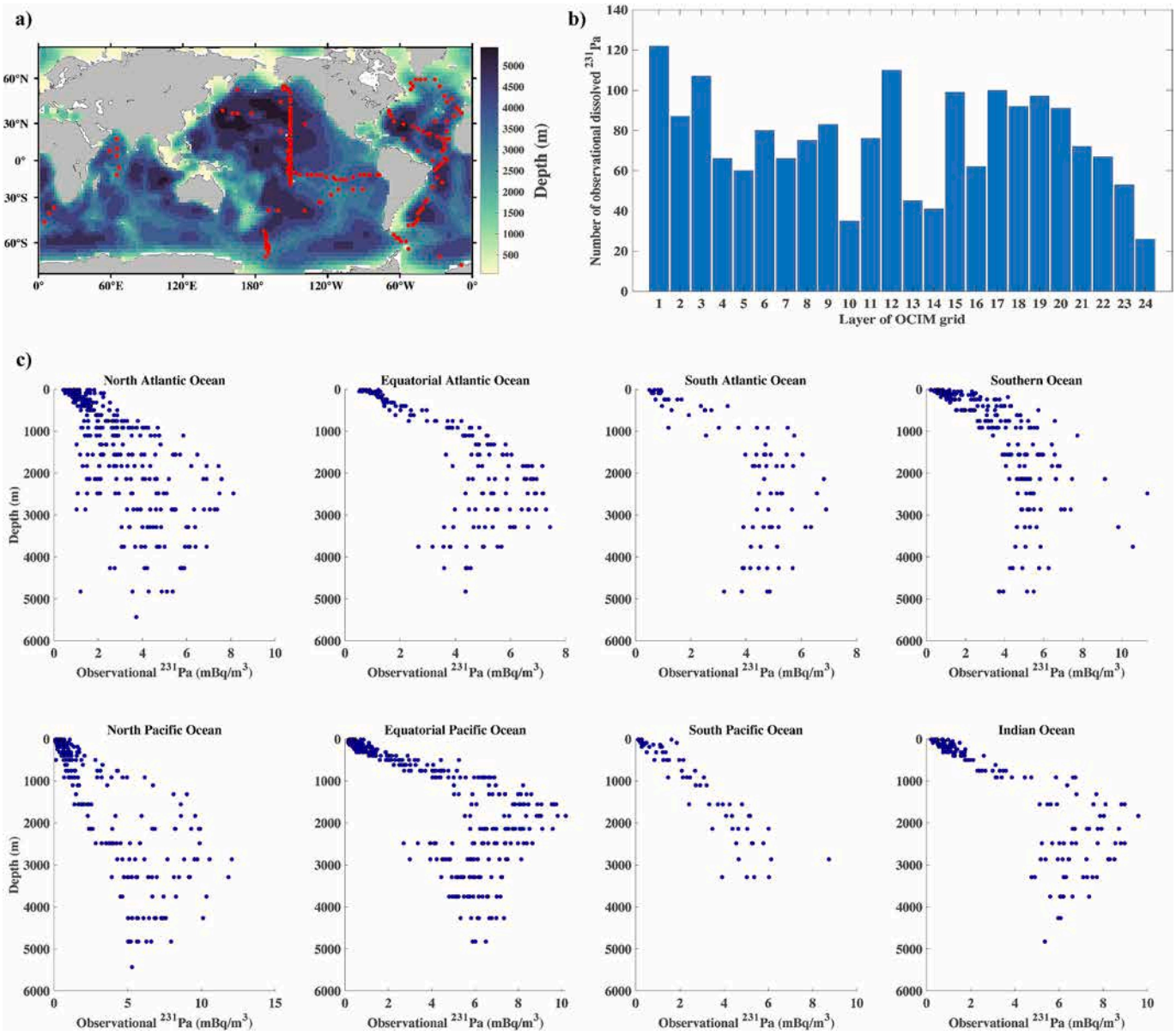

Fig. 1. Spatial distribution of stations with observational data and vertical distribution of observational ^{231}Pa (mBq/m^3) in each sub-basin. a) Global map of depth (color) and distribution of observational data (red points) in the OCIM2 grid. b) Number of observational data in each OCIM vertical layer. c) Global-scale observational dissolved ^{231}Pa profiles. Profiles are shown for selected ocean sub-basins (Teng et al., 2014), whose definitions are shown in the Fig. S1.

The bSi field is modeled from a Si inverse model, in which we model global Si cycle through tracing its two phases in the water column: dissolved silicic acid (DSi) and bSi. The governing equations for the silicon inverse model are as follows,

$$\left[\frac{\mathrm{d}}{\mathrm{dt}}+\mathbf{T}\right]\left[\mathrm{DSi}\right] = -r_{Si:C}\mathrm{G_C}+\kappa_{Si}\left[\mathrm{bSi}\right]+\kappa_g([\mathrm{DSi}]-\overline{[\mathrm{DSi}]_{\mathrm{obs}}})$$

$$\left[\frac{\mathrm{d}}{\mathrm{dt}}+\mathbf{PFD_{bSi}}\right][\mathrm{bSi}] = r_{Si:C}\mathrm{G_C}-\kappa_{Si}[\mathrm{bSi}]$$

$$\kappa_{Si}= at\,\mathrm{e}^{-bt/\mathrm{T}} \quad (3)$$

where $\mathrm{G_C}$ is the DIC assimilation rate described in Wang et al. (2023), which is converted to the DSi assimilation rate by incorporating an optimized Si:C ratio ($r_{(Si:C)}$). The κ_g is a geological restoring parameter, and κ_{Si} is a temperature-dependent dissolution rate of bSi, which is modeled based on the measurements of Erez et al. (1982) and Hurd and Birdwhistell (1983). The *at* and *bt* coded in κ_{Si} are parameters representing energy scales for dissolution. The $\mathbf{PFD}_{\mathrm{bSi}}$ is the PFD operator for bSi, which generates a bSi flux profile following an exponential function with an optimized value d_{bSi} for bSi dissolution length scale:

$$\mathrm{F_{bSi}}(\mathrm{z}) = \mathrm{F_{bSi}}(\mathrm{z_0})\,\mathrm{e}^{(\mathrm{z}-\mathrm{z_0})/d_{bSi}} \quad (4)$$

Like PIC, the d_{bSi} represents the length scale determining bSi dissolution. The exponential formulation generates a vertical flux profile for bSi that exhibits significantly less flux attenuation in the upper water column compared to POC, reflecting the relatively slower dissolution of bSi in shallow waters.

The governing equations of P, C, and Si cycle model are solved based on the optimized parameters shown in the Table S1 to obtain global fields of POC, PIC, and bSi concentrations in units of mmol/m^3. The tracer-tracer (DIP, DSi, DIC and ALK) comparisons are presented in Fig. S3. We then converted particle concentrations to mass fields by multiplying the concentration of each particle type by its molecular

weight (12 g/mol for POC, 100.08 g/mol for PIC, and 67.2 g/mol for bSi, Lam et al., 2018).

2.2.2. Lithogenic particles

We modeled the global distribution of lithogenic particle concentration [Litho] (Fig. S2) using global maps of atmospheric dust deposition flux in units of mg m^{-2} yr^{-1} from Brahney et al. (2015) and Chien et al. (2016), assuming a sinking speed of 200 m/day following Rixen et al. (2019). In addition to gravitational settling, we incorporated a slow dissolution process—an effect often neglected in previous models. This removal rates κ_{Litho} (1/285 $days^{-1}$) is based on the upper bound of the observed residence time of lithogenic particles in the ocean (Ohnemus and Lam, 2015). The equation of lithogenic particle concentrations in our model as follows:

$$\left[\frac{d}{dt}+\mathbf{PFD}_{\mathrm{Litho}}\right][\mathrm{Litho}] = [\mathrm{Dust\ flux}] - \kappa_{Litho}[\mathrm{Litho}] \quad (5)$$

2.3. ^{231}Pa scavenging model

2.3.1. Governing equations for Pa model

We model ^{231}Pa cycle by tracing its five phases in seawater, a "dissolved" phase [Pa_d] that is not associated with particles and four "particulate" phases ([Pa_{POC}], [Pa_{bSi}], [Pa_{PIC}], and [Pa_{Litho}]) that are adsorbed on POC, PIC, bSi, and lithogenic particles, respectively. The governing equations for ^{231}Pa cycling are the following,

$$\left[\frac{d}{dt}+\mathbf{T}\right][Pa_d] = \lambda_{231}\left([^{235}U]-[Pa_d]\right)$$
$$+\kappa_{-1}[Pa_{POC}]+\kappa_{-2}[Pa_{PIC}]+\kappa_{-3}[Pa_{bSi}]+\kappa_{-4}[Pa_{Litho}]$$
$$-(\kappa_1[POC]+\kappa_2[PIC]+\kappa_3[bSi]+\kappa_4[Litho])[Pa_d]$$
$$-[\mathrm{Bottom\ Scavenging}]-[\mathrm{Hydrothermal\ Scavenging}]$$
$$\left[\frac{d}{dt}+\mathbf{PFD}_{\mathbf{POC}}\right][Pa_{POC}] = -(\lambda_{231}+\kappa_{-1})[Pa_{POC}]+\kappa_1[POC][Pa_d]$$
$$\left[\frac{d}{dt}+\mathbf{PFD}_{\mathbf{PIC}}\right][Pa_{PIC}] = -(\lambda_{231}+\kappa_{-2})[Pa_{PIC}]+\kappa_2[PIC][Pa_d]$$
$$\left[\frac{d}{dt}+\mathbf{PFD}_{\mathbf{bSi}}\right][Pa_{bSi}] = -(\lambda_{231}+\kappa_{-3})[Pa_{bSi}]+\kappa_3[bSi][Pa_d]$$
$$\left[\frac{d}{dt}+\mathbf{PFD}_{\mathbf{Litho}}\right][Pa_{Litho}] = -(\lambda_{231}+\kappa_{-4})[Pa_{Litho}]+\kappa_4[Litho][Pa_d] \quad (6)$$

In the model, [Pa_d] is produced via radioactive decay of its conservative parent ^{235}U. The exchange between dissolved and particulate phases is regulated by optimized adsorption and desorption rate constant. [Pa_d] is lost through scavenging onto sinking particles with independent adsorption rate constants for each type of particles (κ_1 for POC, κ_2 for PIC, κ_3 for bSi and κ_4 for Lithogenic particles) and subsequently transported into the deep ocean with sinking particles. Particulate phases of ^{231}Pa can be also released back to the water column via desorption or particle remineralization, which are jointly expressed using three desorption rate constants (κ_{-1} for POC, κ_{-2} for PIC, κ_{-3} for bSi and κ_{-4} for Lithogenic particles.

2.3.2. Parameterization of bottom scavenging

Enhanced scavenging of dissolved ^{231}Pa by particles in nepheloid-layer is a key process regulating its distribution near the seafloor and should therefore be explicitly represented in the model. Currently, there are two main approaches to estimate particle concentrations within the nepheloid layer. The first one is an observation-based approach that uses *in-situ* measurements of particle concentrations in the nepheloid layer to parameterize bottom scavenging. This method has been adopted in previous modeling studies (Lerner et al., 2020; Sasaki et al., 2022; Pöppelmeier et al., 2023; Scheen et al., 2025). However, its global applicability is limited by its spatial coverage of observational data, preventing a global scale parameterization of bottom scavenging. For instance, a global nepheloid-layer particle dataset used in one such study is based on a total of ~ 8800 observations, with large data gaps especially in the Arctic, Southern Ocean, and mid-ocean regions (Gardner et al., 2018a; Gardner et al., 2018b).

As an alternative, previous studies have identified a robust empirical relationship between particle concentrations in the nepheloid layer and surface EKE, which can be derived from satellite altimetry. This relationship between EKE and near-bottom resuspended particle concentrations has been validated across much of the global ocean, although further observations are still needed in regions such as the Kuroshio Extension where benthic particles data are still lacking (Gardner et al., 2017; Gardner et al., 2018a; Gardner et al., 2018b). This linkage between upper ocean dynamics and nepheloid-layer particles provides a spatially continuous proxy for benthic nepheloid-layer particle concentrations, offering a means to incorporate bottom scavenging in data-limited regions. Accordingly, we implemented bottom scavenging using an EKE-based parameterization, in which the intensity of bottom scavenging is proportional to nepheloid-layer particle concentrations estimated from EKE [NEPH.EKE] (Fig. S2e) presented in John et al. (2020). The governing formulation is detailed as follows.

$$[\mathrm{Bottom\ Scavenging}] = \kappa_{BS}[\mathrm{NEPH.EKE}][Pa_d] \quad (7)$$

where the κ_{BS} is bottom scavenging constant optimized in the revision. In the equatorial Pacific, available *in-situ* observations indicate that nepheloid-layer particle concentrations are generally low (Gardner et al., 2018a), despite relatively high values predicted by the satellite EKE–based particle concentrations. This discrepancy suggests that the EKE-based relationship may not be applicable in this region. Consequently, bottom scavenging was disabled in the equatorial Pacific in the model. The result shows that turning off this process leads to modest improvements in simulating near-bottom ^{231}Pa activity. This test implies that bottom scavenging plays a relatively minor role in controlling the ^{231}Pa cycle in the equatorial Pacific, and that the EKE-based method may overestimate the intensity of bottom scavenging in this region.

2.3.3. Parameterization of hydrothermal scavenging

Direct parameterization of distribution of hydrothermal scavenging remains challenging. However, helium-3 (^{3}He), a non-particle-reactive tracer, has been widely used as a proxy to trace the hydrothermal activity, and thus provides an effective tool to implicitly incorporate the hydrothermal scavenging into the model. Existing studies have focused on exploring the relationship between hydrothermal-sourced ^{3}He and dissolved metal concentrations, with limited data on particulate phase (e.g., Resing et al., 2015; Jenkins et al., 2020). A notable exception is the study by Fitzsimmons et al. (2017), which identified an exponential relationship between hydrothermal ^{3}He and particulate metal concentrations along the Southern East Pacific Rise. This suggests that hydrothermal ^{3}He can serve as a valuable proxy for hydrothermal particles.

In this study, we assumed that the hydrothermal particle concentrations have a strong correlation to hydrothermal-sourced ^{3}He flux near vent sources, suggesting that intense hydrothermal particle scavenging occurred in the regions with a high hydrothermal ^{3}He flux. Based on this assumption, we parameterized hydrothermal scavenging by linking the hydrothermal ^{3}He flux to particle scavenging using a tunable coefficient κ_{HS}, which represents the ratio of intensity of hydrothermal scavenging to hydrothermal ^{3}He flux. The hydrothermal ^{3}He flux field ([$^3He_{HS}$]) is derived from a previous estimate in an OCIM framework (Holzer et al., 2017; John et al., 2020), in which the regionally variable differences between seafloor spreading rate and ^{3}He are also considered (Fig. S2g).

$$[\text{Hydrothermal Scavenging}] = \kappa_{HS}\left[{}^{3}\text{He}_{\text{HS}}\right][\text{Pa}_{\text{d}}] \quad (8)$$

Observational evidence shows that hydrothermal-sourced particles like MnO_2 and $Fe(OH)_3$ scavenge ^{231}Pa more effectively than biogenic particles (Pavia et al., 2018). Accordingly, the hydrothermal scavenging in our model is regarded as non-reversible scavenging. This assumption indicates that once [Pa_d] is adsorbed onto particles, it is rapidly transferred to the sediment and permanently removed from the water column, consistent with the assumption adopted in a recent data-constrained ^{230}Th model (Xu and Weber, 2025).

2.4. The optimization

In this study, we optimized a total of 10 parameters (κ_1, κ_{-1}, κ_2, κ_{-2}, κ_3, κ_{-3}, κ_4, κ_{-4}, κ_{BS}, and κ_{HS}) coded in the ^{231}Pa scavenging model using the Bayesian inversion method and the most probable parameter values are presented in Table S2. In this approach, the solutions to our model equations define the tracer fields as implicit functions of the adjustable parameters. We then compare the model fields to the observations to construct a likelihood function. To find the most probable parameter values, we maximize the likelihood of the posterior probability function, which is equivalent to minimizing the negative log-likelihood function. The optimization is conducted using MATLAB's *fminunc* function, which is computationally efficient because we hand coded first (Gradient) and second derivatives (Hessian) of the objective function with respect to the adjustable parameters. By using both the Gradient and Hessian, *fminunc* function can navigate the parameter space more efficiently and converge to the optimal solution faster than methods that rely solely on function evaluations without any derivative information. This approach ensures that the optimization process reliably identifies the best-fitting parameters for our model.

2.5. Sensitivity tests

Based on the best-optimized ^{231}Pa model, we further conducted a set of experiments to explore how reversible, bottom, and hydrothermal scavenging impact the distribution of dissolved ^{231}Pa.

To evaluate the influence of scavenging reversibility on the oceanic distribution of ^{231}Pa, we conducted a sensitivity experiment (NoRev_Exp), in which all desorption processes were disabled by setting the desorption rate constants (κ_{-1}, κ_{-2}, κ_{-3}, and κ_{-4}) to zero. This configuration yielded a purely irreversible scavenging regime that included only adsorption processes while retaining both bottom and hydrothermal scavenging. To further evaluate the contribution of individual particle types to the distribution of ^{231}Pa, we performed four targeted sensitivity tests, 2 × POC.Scav, 2 × PIC.Scav, 2 × bSi.Scav, and 2 × Litho.Scav. In each experiment, the adsorption and desorption rate constants for a single particle class (POC, $CaCO_3$, bSi, and lithogenic particles) were doubled. Additionally, we conducted two sensitivity experiments to isolate the effects of hydrothermal and bottom scavenging by independently excluding each process, resulting in the experiments CTRL (excl. BS) and CTRL (excl. HS).

It is important to note that in all sensitivity experiments (Table S3 and Table S4), all other parameters were held at their optimal values, allowing us to isolate and assess the impact of individual processes. We intentionally chose not to re-optimize the model for these experiments in order to avoid underestimating the contribution of the process being evaluated. For instance, although re-optimized version of the model without bottom scavenging (NOBS) and without hydrothermal scavenging (NOHS) were still able to explain 71 % and 77 % of the observational ^{231}Pa variance, respectively, the non-reoptimized tests showed markedly reduced performance: only 38 % for CTRL (excl. BS) and 76 % for CTRL (excl. HS) (Table S3). This difference highlights that re-optimization can mask the true influence of specific processes by compensating through adjustments in other parameters. In contrast, no such compensation occurs in the CTRL experiment, where all key processes controlling ^{231}Pa distribution are included and the optimized parameters are able to capture the observed distribution without relying on trade-offs among processes.

3. Results

3.1. Optimized global ^{231}Pa scavenging model

3.1.1. Comparison between the optimized model and observations

Overall, the best-optimized model reproduces the observed distribution of dissolved ^{231}Pa well (Fig. 2, Fig. S4, $R^2 = 0.79$, MAE = 0.76 mBq/m^3, $p < 0.001$), demonstrating that the scavenging scheme effectively captures global-scale patterns. However, the model does tend to overestimate ^{231}Pa activity, particularly in the deep Pacific Ocean, where many data points (shown as downward triangles) lie above the 1:1 line. This discrepancy may reflect uncertainties in the underlying circulation fields from OCIM, as well as the sparse spatial coverage of observational data in this region. Despite these limitations, the model shows strong spatial agreement with observations across most of the global ocean, underscoring its value in evaluating the marine ^{231}Pa cycle. However, model performance in the Arctic Ocean remains uncertain due to the exclusion of data from this region and the significant uncertainty in OCIM's circulation representation at high latitudes. Future targeted sampling efforts and advancement in Arctic circulation modeling will be essential for improving ^{231}Pa simulations in polar regions.

We next assessed the scavenging efficiency of each particle type (Table S5). The results indicate that POC is the primary driver of the model's ability to reproduce the observed distribution of ^{231}Pa. When biogenic particles are represented solely by POC, the model explains approximately 68 % of the variance in observed ^{231}Pa data, reflecting the pervasive presence of POC throughout the global ocean. In comparison, simulations using only bSi or PIC explain just 20 % and 10 % of the variance, respectively. Including bSi or PIC alongside POC improves model skill, emphasizing their secondary but supportive roles in reversible scavenging.

Regionally, bSi exerts a particularly strong influence in diatom-rich regions such as the Southern Ocean, while PIC plays a more prominent role in areas with elevated PIC fluxes, such as the subpolar and equatorial Pacific. The inclusion of lithogenic particles yields a modest

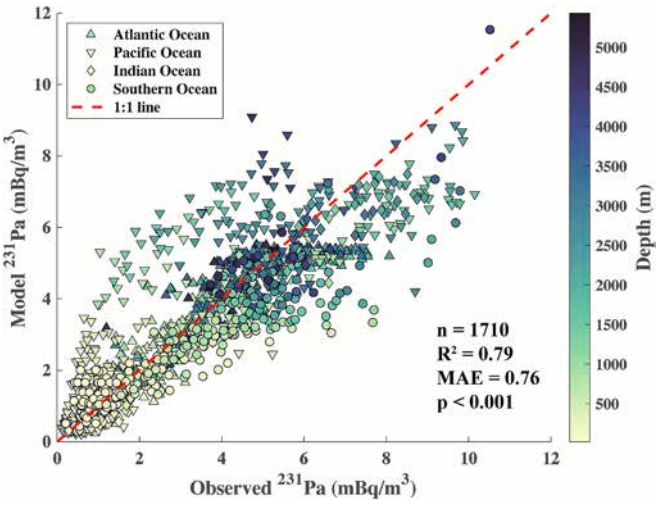

Fig. 2. Tracer-tracer comparisons of dissolved ^{231}Pa activity between model results and observations from BCO-DMO dataset. Each data point is color-coded by depth and shaped according to the ocean basin. The red dashed line represents the 1:1 line, indicating a perfect agreement between the model and observations.

overall improvement may have greater regional significance, particularly in the North Atlantic subtropical gyre, where high dust deposition coincides with low biogenic particle concentrations due to nutrient limitations.

3.1.2. Vertical profiles of ^{231}Pa in the global ocean

Observed ^{231}Pa activity generally increases linearly with depth in the upper ocean, a pattern consistent with reversible scavenging as the dominant removal process. However, this linear trend weakens at greater depths, where ^{231}Pa activity begins to decline. This deviation suggests the influence of additional removal mechanisms, such as bottom and hydrothermal scavenging, that enhance deep-water depletion beyond what reversible scavenging alone can explain. The depletion is particularly pronounced in the Equatorial, Atlantic, and Indian Oceans (Figs. 3b, c and h), likely reflecting intensified benthic and hydrothermal particle concentrations.

Despite these complexities, our model successfully captures the vertical structure of ^{231}Pa across all major ocean basins, showing strong agreement between modeled and observed activity (Fig. 3). A notable exception is the Southern Pacific (Fig. 3g), where model performance is weaker (R^2 = 0.38). These discrepancies likely stem from sparse observational coverage (n = 70) and poorly constrained particle fluxes in this region, which limit the accuracy of scavenging parameterizations.

3.2. Scavenging contribution to ^{231}Pa cycle in the global ocean

Using the optimal scavenging parameters from our ^{231}Pa model (Table S2) and the simulated global distribution of dissolved ^{231}Pa, we quantified the contribution of each particle type to the global ^{231}Pa budget relative to its total production via ^{235}U decay (Table S6). Globally, approximately 71 % of the produced ^{231}Pa is removed through scavenging by biogenic particles, which is relatively lower than the optimized removal of ^{230}Th with a stronger particle affinity (~76 %, Xu and Weber, 2025). Among the removal of ^{231}Pa, bSi exhibits the highest adsorption affinity (~56 %), followed by POC (~ 41 %). However, bSi also has a relatively high desorption rate, indicating that a substantial fraction of adsorbed ^{231}Pa is released back into the dissolved phase during particle sinking. While the rapid desorption of ^{231}Pa from bSi may influence its distribution in the water column, the high burial flux of bSi remains influential, particularly because bSi is not subject to rapid mineralization like POC, allowing ^{23}Pa to be efficiently buried in bSi-rich marine sediments.

In contrast, POC and PIC exhibit lower desorption rates (Table S2), allowing effective transfer of ^{231}Pa into the particulate phase and ultimately to sediment burial. Additionally, bottom scavenging accounts for ~ 24 % of global ^{231}Pa removal, and hydrothermal scavenging contributes ~ 4 %, underscoring their critical roles in enhancing removal near the seafloor and at mid-ocean ridge systems. By comparison, lithogenic particles make only a minor contribution to the global ^{231}Pa budget, reflecting both their limited spatial distribution and the lower affinity of ^{231}Pa for lithogenic material.

4. Discussion

4.1. Sensitivity tests

4.1.1. The impact of reversible scavenging

As shown in Fig. 4, disabling desorption in the NoRev_Exp experiment significantly increases the removal of dissolved ^{231}Pa compared to the CTRL, resulting in widespread underestimation of dissolved ^{231}Pa activity. This effect is most pronounced in the deep ocean, where the cumulative impact of irreversible scavenging leads to progressively stronger depletion with depth. In contrast, the reversible scavenging scheme in CTRL allows for partial release of ^{231}Pa back into the

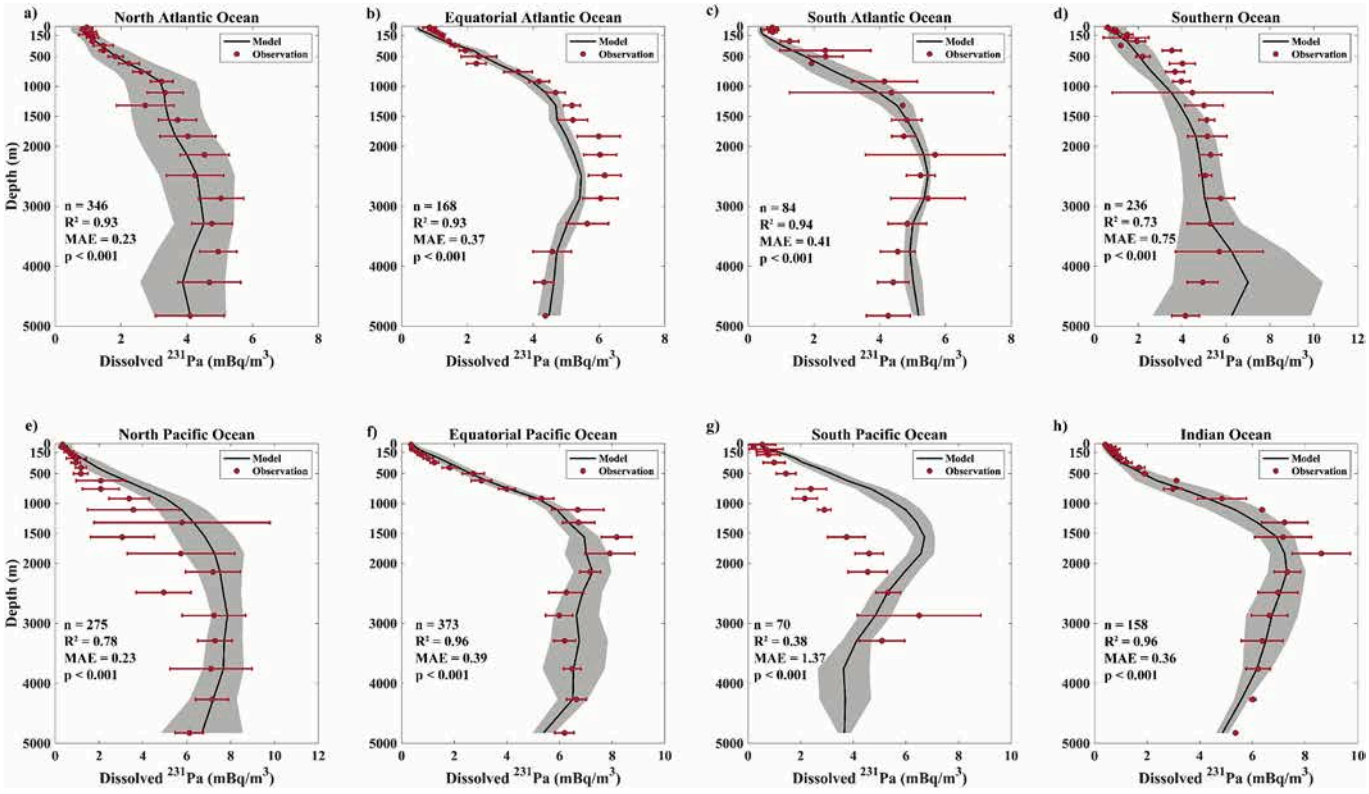

Fig. 3. Basin-average vertical profiles of dissolved ^{231}Pa activity (in mBq/m^3) from our optimal model (CTRL, black lines) and observations (red points with ± 1σ uncertainty), in which bottom scavenging is excluded in the Equatorial Pacific. The number of observations, R^2, MAE and P values are shown in the lower-left corner of each subplot. Profiles are shown for representative sites across major ocean basins: a) North Pacific Ocean. b) Equatorial Pacific Ocean. c) South Pacific Ocean. d) Southern Ocean. e) North Atlantic Ocean. f) Equatorial Atlantic Ocean. g) South Atlantic Ocean. h) Indian Ocean. Sub-basin definitions are shown in the Fig. S1.

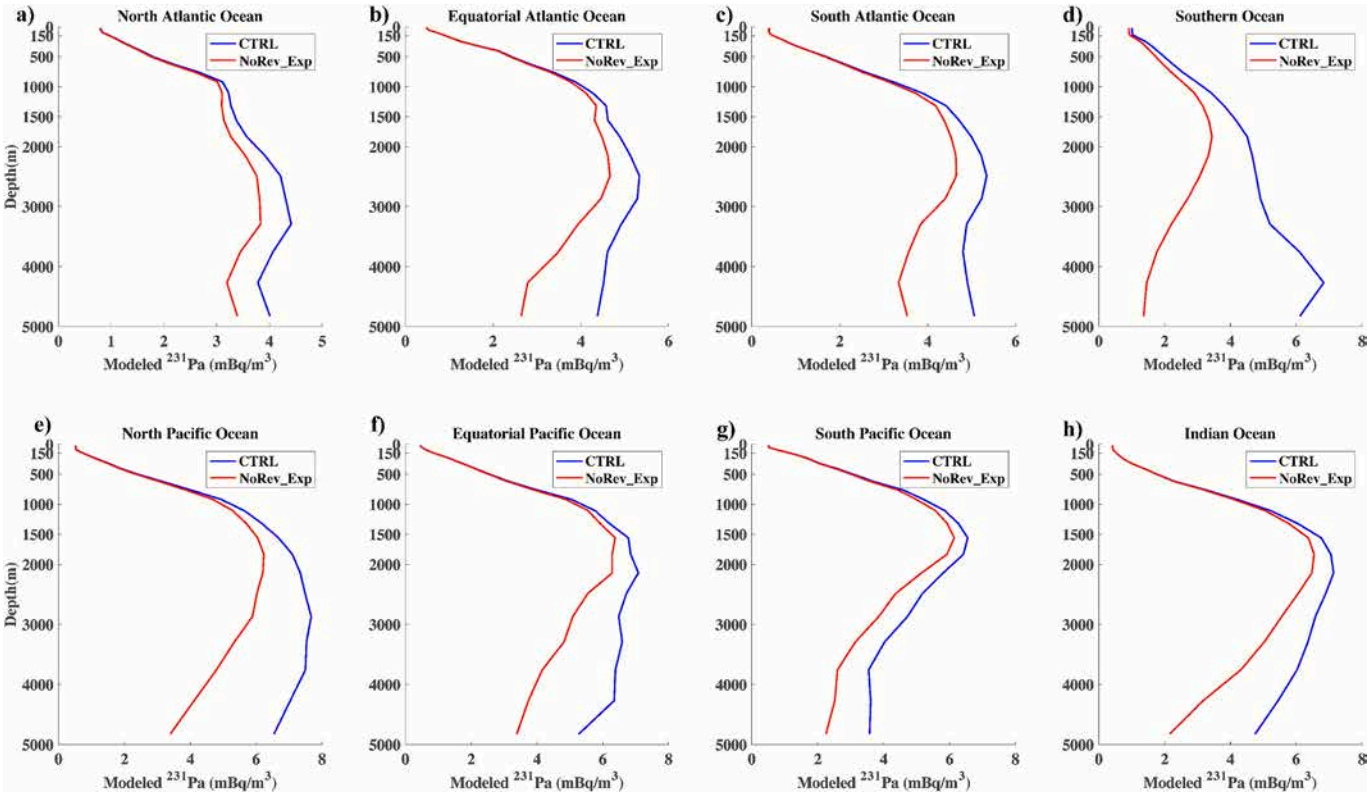

Fig. 4. Basin-average vertical profiles of dissolved ^{231}Pa activity (in mBq/m^3) modeled by the reversible scavenging model (CTRL, blue lines) and the irreversible scavenging model (NoRev_Exp, red lines). Profiles are shown for selected ocean basins: a) North Pacific Ocean. b) Equatorial Pacific Ocean. c) South Pacific Ocean. d) Southern Ocean. e) North Atlantic Ocean. f) Equatorial Atlantic Ocean. g) South Atlantic Ocean. h) Indian Ocean. Sub-basin definitions are shown in the Fig. S1.

dissolved phase during particle setting, buffering its removal from the upper ocean. Consequently, differences between the reversible and irreversible scenarios are minimal in the upper water column across all ocean basins.

A contrasting pattern emerges in the Southern Ocean, where disabling desorption leads to lower ^{231}Pa activity throughout the entire water column compared to the CTRL scenario. In deep waters, this reduction is particularly pronounced, suggesting that reversible scavenging enhances the downward transport of ^{231}Pa, allowing it to reach greater depths before removal. This behavior is likely driven by the dominance of bSi, which has a long dissolution length scale and supports prolonged adsorption–desorption cycling. Additionally, under irreversible scavenging the reduced dissolved ^{231}Pa in the deep Atlantic, where much of the water feeding into the Southern Ocean originates, limits the advective supply of ^{231}Pa to the Southern Ocean, further contributing to the observed surface depletion.

Comparing across ocean basins, water mass age appears to exert a significant influence on the deep-ocean distribution of ^{231}Pa. In the Atlantic, as North Atlantic Deep Water (NADW) forms at high latitudes and flows southward, the effect of reversible scavenging on deep-water ^{231}Pa activity becomes increasingly pronounced. This southward intensification indicates that reversible interactions with sinking particles facilitate the transport of ^{231}Pa to greater depths over time. A similar pattern emerges in the Pacific and Indian Oceans, where disabling desorption leads to excessive particle scavenging and a pronounced underestimation of dissolved ^{231}Pa. This mismatch intensifies along major circulation pathways, increasing from western boundary currents toward the basin interiors, a trend that parallels the age-related behavior observed in the Atlantic. These findings suggest that even in basins characterized by weaker overturning circulation, advective transport pathways modulate the interplay between scavenging processes and tracer distributions (Luo et al., 2021). Together, these results emphasize the critical role of reversible scavenging in combination with large-scale circulation in governing the fate and distribution of particle-reactive tracers like ^{231}Pa in the deep ocean.

4.1.2. *The impact of reversible scavenging intensity*

Across all particle types, increasing scavenging intensity generally leads to a decrease in dissolved ^{231}Pa activity (Fig. 5), reflecting enhanced particle-associated removal. For POC and PIC, which all exhibit low optimized desorption rate, this behavior reinforces their roles as net sinks for ^{231}Pa throughout the water column. As their scavenging intensities increase, modeled ^{231}Pa activity declines accordingly.

However, the vertical influence of each particle type differs. POC plays a dominant role in the upper ocean due to its high adsorption capacity and rapid remineralization, which leads to efficient removal of ^{231}Pa at shallow depths, while PIC exerts a broader vertical impact. Its slower dissolution and low desorption rates allow it to transport adsorbed ^{231}Pa to greater depths, thereby enhancing removal in the deep ocean and facilitating burial in sediments. PIC's contribution in the surface ocean is weaker because it represents a smaller fraction of the total particle mass flux compared to POC. These contrasting behaviors highlight the distinct vertical scavenging profiles of organic versus inorganic carbon particles. These findings are consistent with a recent work showing that particle scavenging acts as a net sink for particle-reactive elements throughout the water column (Du et al., 2025).

In contrast, an intriguing exception is observed for bSi. When the reversible scavenging rates of bSi are doubled, the model unexpectedly predicts a slight increase in deep-water ^{231}Pa activity, particularly in regions with high bSi flux such as the Southern Ocean and North Pacific, where diatoms are abundant. This behavior suggests that stronger bSi scavenging enhances the downward transport of bSi-bound ^{231}Pa, which is subsequently released via desorption at depth, elevating dissolved

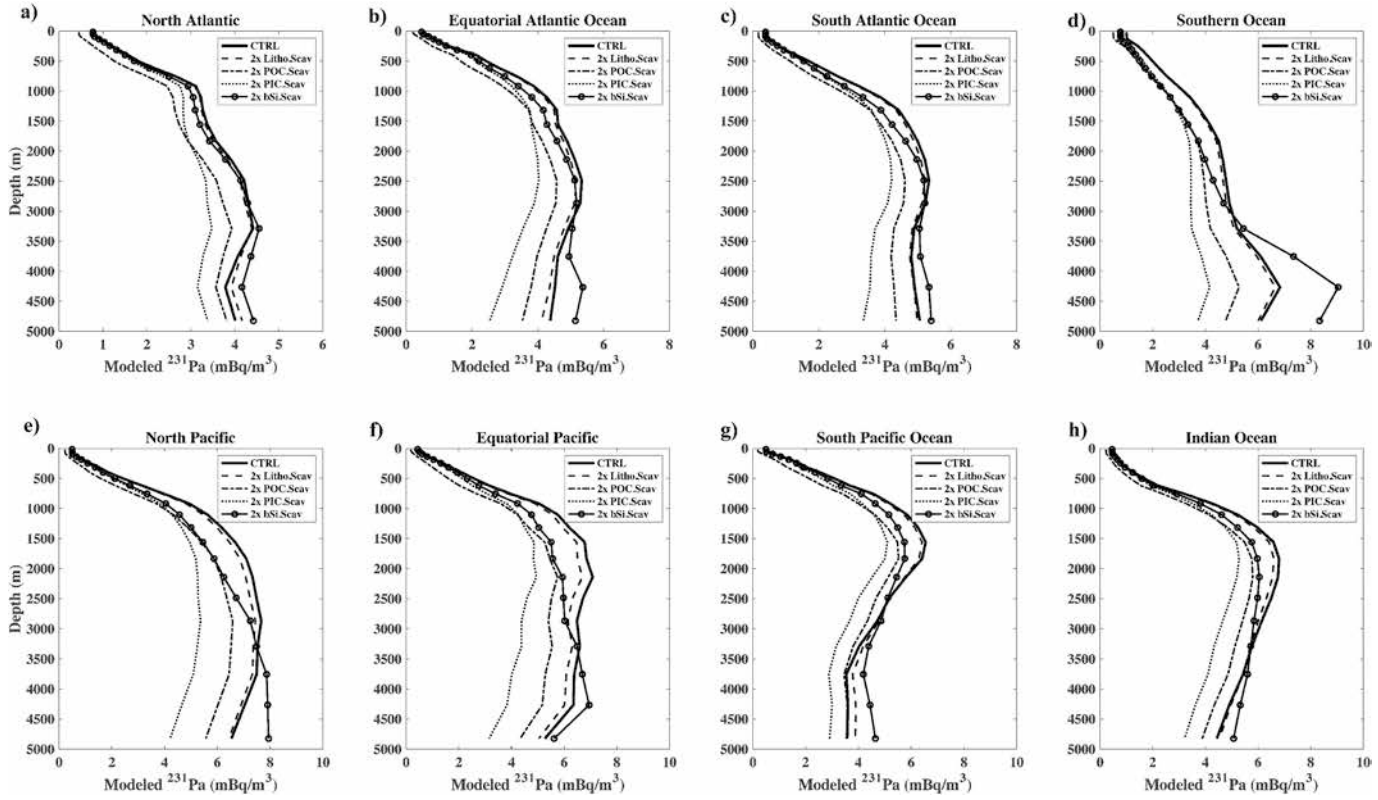

Fig. 5. Basin-average profiles of dissolved ^{231}Pa activity (in mBq/m^3) under varying reversible scavenging intensities of four particle types in eight major ocean regions. The black solid lines represent the CTRL (best-optimized model). Dashed and dotted lines represent sensitivity experiments where the reversible scavenging (adsorption and desorption rates) for individual particle types (POC, PIC, bSi and Litho) was doubled ("2 × Particle type. Scav"). No parameter re-optimization was applied. a) North Pacific Ocean. b) Equatorial Pacific Ocean. c) South Pacific Ocean. d) Southern Ocean. e) North Atlantic Ocean. f) Equatorial Atlantic Ocean. g) South Atlantic Ocean. h) Indian Ocean. Sub-basin definitions are shown in the Fig. S1.

^{231}Pa activity in the deep ocean. A similar, though weaker, pattern is observed for lithogenic particles in some regions (Figs. 5a, g, h), where enhanced scavenging intensity also results in slightly higher deep-water ^{231}Pa. These results can be explained by the non-regenerative nature of both bSi and lithogenic particles: unlike POC, they do not dissolve or degrade rapidly in the water column. As a result, they can effectively transport adsorbed ^{231}Pa to depth, where desorption contributes to elevated deep-ocean activity of ^{231}Pa.

4.1.3. The impact of bottom scavenging

To investigate the role of bottom scavenging in shaping the distribution of ^{231}Pa, we performed a sensitivity experiment in which bottom scavenging was disabled from the control configuration, referred to as CTRL (excl. BS). Removing this process substantially degraded the model's ability to reproduce observed ^{231}Pa distributions, with the R^2 value dropping from 0.79 (CTRL) to just 0.38 (Table S3). This stark reduction highlights that omitting this process leads to large mismatches with observations, particularly in the deep ocean (Fig. 6).

These results underscore the importance of bottom scavenging in controlling the behavior of particle-reactive tracers, especially in the deep ocean and along continental margins where resuspended particle concentrations are high. They also support the use of satellite-derived EKE as a proxy for parameterizing bottom scavenging. However, this approach is inherently limited to present-day conditions due to its dependence on satellite observations. Extending the model to paleoclimate or future scenarios will require alternative approaches to represent benthic particle dynamics.

Despite uncertainties related to the heterogeneous nature of nepheloid layer particles, our results demonstrate that EKE-based parameterizations provide an effective framework for capturing bottom scavenging of particle-reactive elements in the modern ocean, substantially improving model performance at depth.

4.1.4. The impact of hydrothermal scavenging

In the CTRL (Excl. HS) simulation, where hydrothermal scavenging was disabled, the model still successfully explained a large fraction of the observed variability in dissolved ^{231}Pa (R^2 = 0.76), only slightly lower than the CTRL simulation (R^2 = 0.79). This minor reduction suggests that hydrothermal scavenging plays a relatively limited role in shaping the global-scale distribution of ^{231}Pa. Vertical profiles from CTRL (Excl. HS) are also broadly similar to those from the full CTRL simulation (black lines) across most ocean basins (Fig. 6), further supporting its minimal global impact compared to bottom scavenging.

However, notable deviations occur in regions near mid-ocean ridges, where active hydrothermal venting enhances local particle fluxes. In these regions, the absence of hydrothermal scavenging leads to significant overestimation of dissolved ^{231}Pa near the seafloor, underscoring the important role hydrothermal particles play in promoting localized removal. In some regions, the magnitude of hydrothermal scavenging at depth is comparable to, or even greater than, bottom scavenging (Fig. S5). Thus, while hydrothermal scavenging has a limited effect on the global ^{231}Pa budget, its regional influence in hydrothermally active areas is substantial and, in many cases, may exceed the impact of bottom scavenging.

4.2. Potential role of Boundary scavenging

Boundary scavenging refers to the intensified removal of particle-reactive elements like ^{231}Pa near continental margins, where elevated particle concentrations and steep dissolved concentration gradients

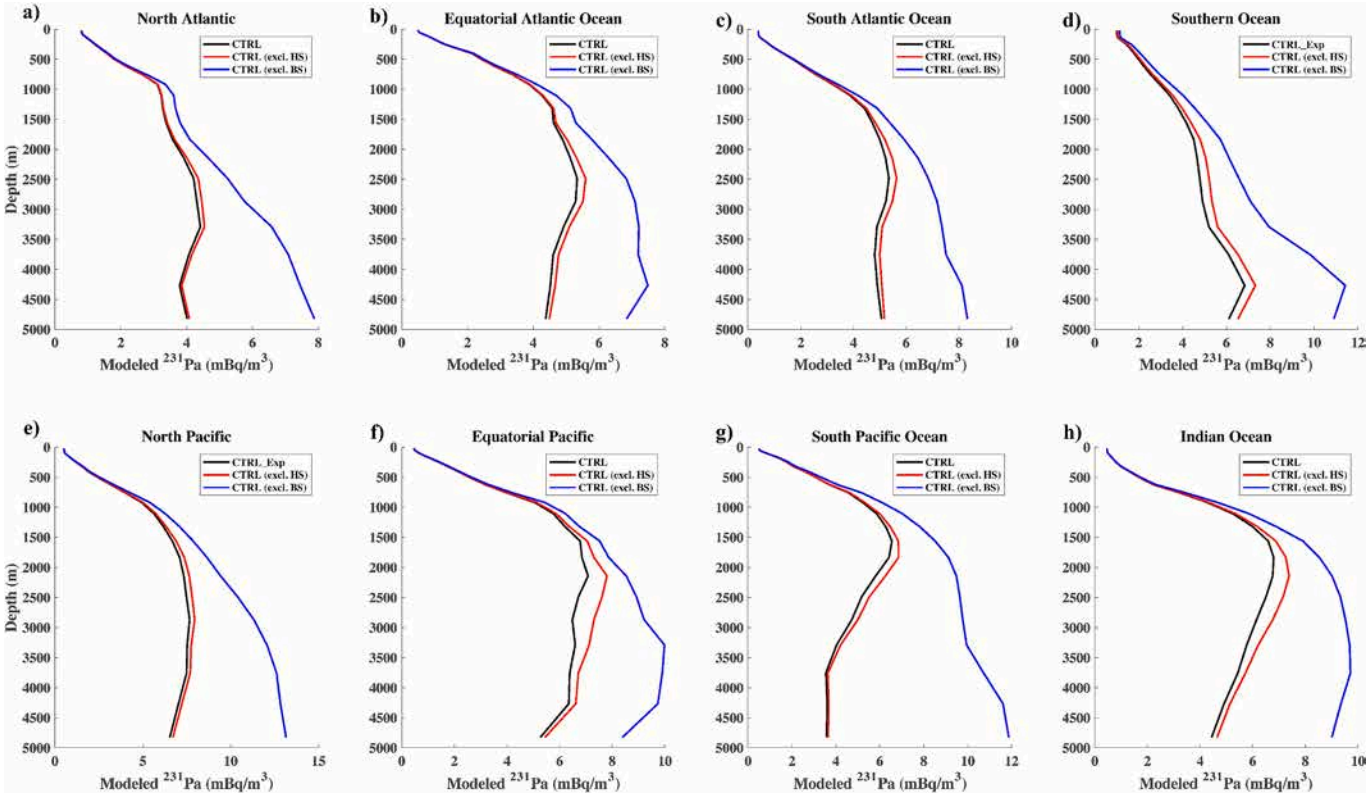

Fig. 6. Basin-average profiles of dissolved ^{231}Pa activity in different sensitivity experiments. Black line: CTRL, Red line: CTRL (excl. HS), Blue line: CTRL (excl. BS). In CTRL (excl. BS) and CTRL (excl. HS), the corresponding scavenging process was respectively excluded, while all other model parameters were held fixed from the control run without re-optimization. Sub-basin definitions are shown in the Fig. S1.

drive lateral transport and mixing toward regions of high particle flux. The influence of boundary scavenging is particularly pronounced in the Atlantic Ocean and has been explicitly parameterized in the previous model (Rempfer et al., 2017). Although our model does not explicitly parameterize boundary scavenging, it is implicitly represented through the circulation model (OCIM2), which governs the lateral and vertical advection and diffusion of dissolved tracers. The validity of this implicit representation is supported by the strong correlation between modeled and observed ^{231}Pa activity across the Atlantic basins (Fig. 3a-c). This suggests that, under sufficient observational constraints and realistic transport representation, an explicit boundary scavenging term may not be essential for accurately simulating the ^{231}Pa distribution in the Atlantic.

Observations have also reported the impact of boundary scavenging in some high-latitude regions, such as the Southern Ocean and the Subarctic North Pacific and Arctic Ocean (Hayes et al., 2013; Grenier et al., 2019; Gdaniec et al., 2020). However, the modeled ^{231}Pa in these regions are poorly constrained due to sparse observational data. Notably, these areas also coincide with regions where OCIM2 exhibits the highest uncertainties (DeVries and Holzer, 2019). Consequently, any misrepresentation of lateral transport in these regions may lead to biases in the estimated intensity of boundary scavenging. Therefore, while our model accounts for boundary scavenging through its transport dynamics, future work could benefit from more explicit schemes or observationally derived constraints to quantify margin-specific particle fluxes. This would allow a more detailed investigation of the relative roles of boundary scavenging versus deep interior removal processes in shaping the global ^{231}Pa distribution.

4.3. Implications of particle scavenging on particle-reactive elements

Particle scavenging has been recognized as a key process vertically redistributing trace metal in the modern ocean (Tagliabue et al., 2010; Tagliabue et al., 2019; Roshan et al., 2020; Lanning et al., 2023). One major impact of particle scavenging on biogeochemical cycle is the depletion of particle-reactive micronutrients in surface waters, which plays a critical role in regulating primary production. For example, scavenging process strongly influences the oceanic cycle of dissolved iron (dFe), which is rapidly removed from the water column, leading to low iron concentration and severe iron limitation. This removal limits nutrient assimilation by phytoplankton, ultimately lowering primary productivity and reducing the ability to sequestrate atmospheric CO_2 via biological pump (Tagliabue et al., 2017). However, current biogeochemical models inadequately represent particle scavenging, leading to substantial uncertainty in estimates of micronutrient bioavailability (Tagliabue et al., 2016). Our results highlight the importance of not only total particle mass, but also the distinct roles of specific particle types (e.g., POC, PIC, bSi, and lithogenic particles of our model) in governing oceanic distribution of particle-reactive elements. Recent studies also reveal that dFe is more likely scavenged by authigenic minerals than by biogenic particles, highlighting the need to account for authigenic minerals in iron scavenging models (Tagliabue et al., 2023). This distinction is particularly important for particle-reactive trace metals, whose distributions depend not only on total particle concentrations but also on the specific affinities of different particle types, which can vary significantly.

4.4. Limitations and future work

Despite the strengths of our data-constrained model, several limitations remain that warrant further investigation. First, the accuracy of the model is inherently tied to the spatial and temporal resolution of the circulation field, as well as the quality and coverage of observational data. Future studies would benefit from applying a higher-resolution

version of OCIM and expanding the observational dataset, particularly in under-sampled regions such as the Southern Ocean. Second, our use of indirect proxy-based approaches to parameterize bottom and hydrothermal scavenging introduces uncertainties that merit closer examination. The representation of bottom scavenging, for instance, is constrained by temporal coverage of satellite data. Hydrothermal scavenging in our model is similarly driven by locally enhanced removal near mid-ocean ridges and subsequent transport of ^{231}Pa-depleted waters by OCIM. However, the assumed empirical relationship between ^{3}He flux and ^{231}Pa depletion may not be universally applicable. For example, recent work in the Pacific Tropical Gyres has shown elevated ^{3}He without hydrothermal depletion in ^{231}Pa (Redmond et al., 2025). Finally, although our model simulates water-column scavenging processes, it does not explicitly represent ^{231}Pa burial in marine sediments. This omission limits our ability to quantify how distinct scavenging pathways ultimately influence sedimentary fluxes. Incorporating sedimentary sinks in future model iterations will be essential for evaluating the role of scavenging processes in controlling benthic ^{231}Pa burial.

Our modeling framework for ^{231}Pa is broadly applicable to other particle-reactive trace elements in the ocean. For instance, this approach can be readily adapted to simulate ^{230}Th, which shares similar sources and scavenging pathways with ^{231}Pa but differs in particle affinity and residence time. Future development of a coupled ^{231}Pa–^{230}Th model would enable a more comprehensive examination of how reversible, bottom, and hydrothermal scavenging jointly regulate the distribution and sedimentary fluxes of these elements in the modern ocean. Moreover, a mechanistic understanding of how these processes affect the relative deposition rates of ^{231}Pa and ^{230}Th would enhance the interpretation of their sedimentary ratio as a proxy for reconstructing past ocean circulation.

5. Conclusions

In this study, we present a global simulation of the ^{231}Pa cycle using a data-constrained scavenging model that explicitly resolves reversible, bottom, and hydrothermal scavenging processes. The model incorporates three major biogenic particle types and lithogenic particles with independently optimized adsorption and desorption parameters. To capture localized scavenging intensities, we introduced a novel approach using nepheloid-layer particle concentrations inferred from satellite-derived EKE and hydrothermal ^{3}He fluxes as proxies for bottom and hydrothermal scavenging, respectively. This enhanced framework successfully reproduces the observed global distributions and vertical profiles of dissolved ^{231}Pa, achieving a high degree of correlation with observational data ($R^2 = 0.79$).

Our results demonstrate that reversible scavenging accounts for 74 % of global dissolved ^{231}Pa removal, underscoring its critical role in shaping large-scale spatial patterns. Sensitivity tests reveal distinct particle-specific impacts: POC and PIC consistently act as net sinks throughout the water column, whereas bSi, due to its higher desorption rate, redistributes dissolved ^{231}Pa to greater depths, highlighting its unique role in modulating deep-water inventories. Bottom scavenging emerges as a significant contributor (24 % of global removal), particularly in reducing deep-water ^{231}Pa activity and improving model skill, while hydrothermal scavenging, though globally minor (4 %), exerts important localized effects near ridge systems.

Beyond improving our ability to simulate ^{231}Pa as a quantitative tracer of particle dynamics, this work offers broader insights into particle-mediated export and redistribution processes in the ocean. Since particle scavenging also influences the distribution and bioavailability of essential trace elements like iron, our mechanistically informed and data-constrained model framework provides a valuable tool for advancing the representation of particle-tracer interactions in ocean biogeochemical models. These advances are critical for improving predictive understanding of particle-driven nutrient cycles and their role in regulating marine productivity and carbon export in the modern and past oceans (Costa et al., 2016; Costa et al., 2017).

Data availability

Codes, observational dissolved ^{231}Pa and outputs of Pa inverse model presented in this study are available through Zenodo at https://doi.org/10.5281/zenodo.17832133.

CRediT authorship contribution statement

Jing-Shan Meng: Writing – original draft, Visualization, Methodology, Investigation, Formal analysis. **Wei-Lei Wang:** Writing – review & editing, Supervision, Methodology, Formal analysis, Conceptualization.

Declaration of competing interest

The authors declare that they have no competing financial interests or personal relationships that could have appeared to influence the work reported in this paper.

Acknowledgments

This study has been conducted using E.U. Copernicus Marine Service Information. We sincerely thank the many scientists and researchers who contributed to the collection of ^{231}Pa and nutrient measurements. Our gratitude also extends to the institutions and individuals who maintain the public data repositories, including GEOTRACES, GLODAP, WOA, and the Ocean Productivity website hosted by Oregon State University. Special thanks go to Dr. Frank J. Pavia for compiling the BCO-DMO ^{231}Pa dataset, which significantly contributed to this work. W.-L.W and J.-S.M were supported by the National Key Research and Development Program of China (NKPs, grant ID: 2023YFF0805004), the National Natural Science Foundation of China (NSFC, grant ID: 42476031), and the Natural Science Foundation of Fujian Province of China (Grant ID: 2023J02001).

Appendix A. Supplementary material

The Supplementary Material includes Supplementary Figures 1–5 and Tables 1–5. Fig. S1 shows the sub-basin definitions used in this study. Figure S2 shows global distribution of particle flux, EKE-based particle concentrations and hydrothermal-sourced ^{3}He flux. Figure S3 shows comparisons between the biogeochemical inverse model and observations. Figure S4 shows basin-averaged meridional sections of observational and modeled dissolved ^{231}Pa activity. Figure S5 shows vertical profiles of hydrothermal scavenging intensity and bottom scavenging intensity. Table S1 and Table S2 list the optimized parameter values coded in the biogeochemical inverse model and ^{231}Pa inverse model, respectively. Table S3, Table S4 and Table S5 summarize sensitivity tests conducted in this study. Table S6 presents optimized budget of global ^{231}Pa cycle. Supplementary material to this article can be found online at https://doi.org/10.1016/j.gca.2025.11.046.

References

Anderson, R.F., Bacon, M.P., Brewer, P.G., 1983a. Removal of ^{230}Th and ^{231}Pa from the open ocean. Earth Planet. Sci. Lett. 62 (1), 7–23.
Anderson, R.F., Bacon, M.P., Brewer, P.G., 1983b. Removal of ^{230}Th and ^{231}Pa at ocean margins. Earth Planet. Sci. Lett. 66, 73–90.
Bacon, M.P., 1988. Tracers of chemical scavenging in the ocean: boundary effects and large-scale chemical fractionation. *Philosophical transactions of the Royal Society of London. Series a, Mathematical and Physical*. Sciences 325 (1583), 147–160.
Bacon, M.P., Anderson, R.F., 1982. Distribution of thorium isotopes between dissolved and particulate forms in the deep sea. J. Geophys. Res. Oceans 87 (C3), 2045–2056.
Biscaye, P.E., Eittreim, S.L., 1977. Suspended particulate loads and transports in the nepheloid layer of the abyssal Atlantic Ocean. Mar. Geol. 23 (1–2), 155–172.

Brahney, J., Mahowald, N., Ward, D.S., Ballantyne, A.P., Neff, J.C., 2015. Is atmospheric phosphorus pollution altering global alpine Lake stoichiometry? Global Biogeochem. Cycles 29 (9), 1369–1383.
Chase, Z., Anderson, R.F., Fleisher, M.Q., Kubik, P.W., 2002. The influence of particle composition and particle flux on scavenging of Th, Pa and Be in the ocean. Earth Planet. Sci. Lett. 204 (1–2), 215–229.
Chase, Z., Anderson, R.F., Fleisher, M.Q., Kubik, P.W., 2003. Scavenging of ^{230}Th, ^{231}Pa and ^{10}Be in the Southern Ocean (SW Pacific sector): the importance of particle flux, particle composition and advection. Deep Sea Res. Part II 50 (3–4), 739–768.
Chen, S.Y.S., Marchal, O., Lerner, P.E., McCorkle, D.C., van der Loeff, M.M.R., 2021. On the cycling of ^{231}Pa and ^{230}Th in benthic nepheloid layers. Deep Sea Res. Part I 177, 103627.
Chien, C.T., Mackey, K.R., Dutkiewicz, S., Mahowald, N.M., Prospero, J.M., Paytan, A., 2016. Effects of african dust deposition on phytoplankton in the western tropical Atlantic Ocean off Barbados. Global Biogeochem. Cycles 30 (5), 716–734.
Cochran, J.K., Livingston, H.D., Hirschberg, D.J., Surprenant, L.D., 1987. Natural and anthropogenic radionuclide distributions in the northwest Atlantic Ocean. Earth Planet. Sci. Lett. 84 (2–3), 135–152.
Costa, K.M., McManus, J.F., Anderson, R.F., Ren, H., Sigman, D.M., Winckler, G., Ravelo, A.C., 2016. No iron fertilization in the equatorial Pacific Ocean during the last ice age. Nature 529 (7587), 519–522.
Costa, K.M., Jacobel, A.W., McManus, J.F., Anderson, R.F., Winckler, G., Thiagarajan, N., 2017. Productivity patterns in the equatorial Pacific over the last 30,000 years. Global Biogeochem. Cycles 31 (5), 850–865.
Costa, K.M., Hayes, C.T., Anderson, R.F., Pavia, F.J., Bausch, A., Deng, F., Zhou, Y., 2020. ^{230}Th normalization: New insights on an essential tool for quantifying sedimentary fluxes in the modern and Quaternary ocean. Paleoceanogr. Paleoclimatol. 35 (2), e2019PA003820.
Deng, F., Henderson, G.M., Castrillejo, M., Perez, F.F., Steinfeldt, R., 2018. Evolution of ^{231} Pa and ^{230} Th in overflow waters of the North Atlantic. Biogeosciences 15 (23), 7299–7313.
DeVries, T., Holzer, M., 2019. Radiocarbon and helium isotope constraints on deep ocean ventilation and mantle-3He sources. J. Geophys. Res. Oceans 124 (5), 3036–3057.
Du, J., Haley, B.A., McManus, J., Blaser, P., Rickli, J., Vance, D., 2025. Abyssal seafloor as a key driver of ocean trace-metal biogeochemical cycles. Nature 1–8.
Erez, J., Takahashi, K., Honjo, S., 1982. In-situ dissolution experiment of Radiolaria in the central North Pacific Ocean. Earth Planet. Sci. Lett. 59 (2), 245–254.
Ewing, M., Thorndike, E.M., 1965. Suspended matter in deep ocean water. Science 147 (3663), 1291–1294.
Fitzsimmons, J.N., John, S.G., Marsay, C.M., Hoffman, C.L., Nicholas, S.L., Toner, B.M., Sherrell, R.M., 2017. Iron persistence in a distal hydrothermal plume supported by dissolved–particulate exchange. Nat. Geosci. 10 (3), 195–201.
Fu, W., Wang, W.L., 2022. Biogeochemical equilibrium responses to maximal productivity in high nutrient low chlorophyll regions. J. Geophys. Res. Biogeo. 127 (5), e2021JG006636.
Gardner, W.D., Tucholke, B.E., Richardson, M.J., Biscaye, P.E., 2017. Benthic storms, nepheloid layers, and linkage with upper ocean dynamics in the western North Atlantic. Mar. Geol. 385, 304–327.
Gardner, W.D., Richardson, M.J., Mishonov, A.V., 2018a. Global assessment of benthic nepheloid layers and linkage with upper ocean dynamics. Earth Planet. Sci. Lett. 482, 126–134.
Gardner, W.D., Richardson, M.J., Mishonov, A.V., Biscaye, P.E., 2018b. Global comparison of benthic nepheloid layers based on 52 years of nephelometer and transmissometer measurements. Prog. Oceanogr. 168, 100–111.
Gdaniec, S., Roy-Barman, M., Levier, M., Valk, O., van Der Loeff, M.R., Foliot, L., Andersson, P.S., 2020. ^{231}Pa and ^{230}Th in the Arctic Ocean: Implications for boundary scavenging and ^{231}Pa-^{230}Th fractionation in the Eurasian Basin. Chem. Geol. 532, 119380.
German, C.R., Higgs, N.C., Thomson, J., Mills, R., Elderfield, H., Blusztajn, J., Bacon, M. P., 1993. A geochemical study of metalliferous sediment from the TAG Hydrothermal Mound, 26° 08′ N, Mid-Atlantic Ridge. J. Geophys. Res. Solid Earth 98 (B6), 9683–9692.
German, C.R., Bourles, D.L., Brown, E.T., Hergt;, J., Colley, S., Higgs, N.C., Yiou, F., 1997. Hydrothermal scavenging on the Juan de Fuca Ridge: ^{230}Thxs, ^{10}Be, and REEs in ridge-flank sediments. Geochim. Cosmochim. Acta 61 (19), 4067–4078.
Goldberg, E.D., 1954. Marine geochemistry 1. Chemical scavengers of the sea. J. Geol. 62 (3), 249–265.
Grenier, M., François, R., Soon, M., Rutgers van der Loeff, M., Yu, X., Valk, O., Allen, S.E., 2019. Changes in circulation and particle scavenging in the Amerasian Basin of the Arctic Ocean over the last three decades inferred from the water column distribution of geochemical tracers. J. Geophys. Res. Oceans 124 (12), 9338–9363.
Gu, S., Liu, Z., 2017. ^{231}Pa and ^{230}Th in the ocean model of the Community Earth System Model (CESM1. 3). Geosci. Model Dev. 10 (12), 4723–4742.
Hayes, C.T., Anderson, R.F., Jaccard, S.L., François, R., Fleisher, M.Q., Soon, M., Gersonde, R., 2013. A new perspective on boundary scavenging in the North Pacific Ocean. Earth Planet. Sci. Lett. 369, 86–97.
Hayes, C.T., Anderson, R.F., Fleisher, M.Q., Huang, K.F., Robinson, L.F., Lu, Y., Moran, S. B., 2015a. ^{230}Th and ^{231}Pa on GEOTRACES GA03, the US GEOTRACES North Atlantic transect, and implications for modern and paleoceanographic chemical fluxes. Deep Sea Res. Part II 116, 29–41.
Hayes, C.T., Anderson, R.F., Fleisher, M.Q., Vivancos, S.M., Lam, P.J., Ohnemus, D.C., Moran, S.B., 2015b. Intensity of Th and Pa scavenging partitioned by particle chemistry in the North Atlantic Ocean. Mar. Chem. 170, 49–60.
Henderson, G.M., Anderson, R.F., 2003. The U-series toolbox for paleoceanography. Rev. Mineral. Geochem. 52 (1), 493–531.
Holzer, M., DeVries, T., Bianchi, D., Newton, R., Schlosser, P., Winckler, G., 2017. Objective estimates of mantle ^{3}He in the ocean and implications for constraining the deep ocean circulation. Earth Planet. Sci. Lett. 458, 305–314.
Hurd, D.C., Birdwhistell, S., 1983. On producing a more general model for biogenic silica dissolution. Am. J. Sci. 283 (1), 1–28.
Jenkins, W.J., Hatta, M., Fitzsimmons, J.N., Schlitzer, R., Lanning, N.T., Shiller, A., Cahill, K.L., 2020. An intermediate-depth source of hydrothermal 3He and dissolved iron in the North Pacific. Earth Planet. Sci. Lett. 539, 116223.
John, S.G., Liang, H., Weber, T., DeVries, T., Primeau, F., Moore, K., Taburet, G., 2020. AWESOME OCIM: a simple, flexible, and powerful tool for modeling elemental cycling in the oceans. Chem. Geol. 533, 119403.
Kriest, I., Oschlies, A., 2008. On the treatment of particulate organic matter sinking in large-scale models of marine biogeochemical cycles. Biogeosciences 5 (1), 55–72.
Ku, T.L., Mathieu, G.G., Knauss, K.G., 1977. Uranium in open ocean: concentration and isotopic composition. Deep Sea Res. 24 (11), 1005–1017.
Lam, P.J., Lee, J.M., Heller, M.I., Mehic, S., Xiang, Y., Bates, N.R., 2018. Size-fractionated distributions of suspended particle concentration and major phase composition from the US GEOTRACES Eastern Pacific Zonal Transect (GP16). Mar. Chem. 201, 90–107.
Lanning, N.T., Jiang, S., Amaral, V.J., Mateos, K., Steffen, J.M., Lam, P.J., Fitzsimmons, J.N., 2023. Isotopes illustrate vertical transport of anthropogenic Pb by reversible scavenging within Pacific Ocean particle veils. Proc. Natl. Acad. Sci. 120 (23), e2219688120.
Lauvset, S.K., Lange, N., Tanhua, T., Bittig, H.C., Olsen, A., Kozyr, A., Key, R.M., 2021. An updated version of the global interior ocean biogeochemical data product, GLODAPv2. 2021. Earth Syst. Sci. Data Discuss. 2021, 1–32.
Lerner, P., Marchal, O., Lam, P.J., Gardner, W., Richardson, M.J., Mishonov, A., 2020. A model study of the relative influences of scavenging and circulation on ^{230}Th and 231Pa in the western North Atlantic. Deep Sea Res. Part I 155, 103159.
Levier, M., Roy-Barman, M., Foliot, L., Dapoigny, A., Lacan, F., 2023. Distribution of Pa in the Atlantic sector of the Southern Ocean: Tracking scavenging during water mass mixing along neutral density surfaces. Deep Sea Res. Part I 194, 103951.
Lund, D.C., Pavia, F.J., Seeley, E.I., McCart, S.E., Rafter, P.A., Farley, K.A., Anderson, R. F., 2019. Hydrothermal scavenging of 230Th on the Southern East Pacific Rise during the last deglaciation. Earth Planet. Sci. Lett. 510, 64–72.
Luo, Y., Lippold, J., Allen, S.E., Tjiputra, J., Jaccard, S.L., Francois, R., 2021. The influence of deep water circulation on the distribution of ^{231}Pa and ^{230}Th in the Pacific Ocean. Earth Planet. Sci. Lett. 554, 116674.
Middleton, J.L., Mukhopadhyay, S., Costa, K.M., Pavia, F.J., Winckler, G., McManus, J.F., Huybers, P.J., 2020. The spatial footprint of hydrothermal scavenging on 230ThXS-derived mass accumulation rates. Geochim. Cosmochim. Acta 272, 218–234.
Moran, S.B., Shen, C.C., Weinstein, S.E., Hettinger, L.H., Hoff, J.H., Edmonds, H.N., Edwards, R.L., 2001. Constraints on deep water age and particle flux in the equatorial and South Atlantic Ocean based on seawater ^{231}Pa and ^{230}Th data. Geophys. Res. Lett. 28 (18), 3437–3440.
Moran, S.B., Shen, C.C., Edmonds, H.N., Weinstein, S.E., Smith, J.N., Edwards, R.L., 2002. Dissolved and particulate ^{231}Pa and ^{230}Th in the Atlantic Ocean: constraints on intermediate/deep water age, boundary scavenging, and ^{231}Pa/^{230}Th fractionation. Earth Planet. Sci. Lett. 203 (3–4), 999–1014.
Ng, H.C., Robinson, L.F., Rowland, G.H., Chen, S.S., McManus, J.F., 2020. Coupled analysis of seawater and sedimentary ^{231}Pa/^{230}Th in the tropical Atlantic. Mar. Chem. 227, 103894.
Ohnemus, D.C., Lam, P.J., 2015. Cycling of lithogenic marine particles in the US GEOTRACES North Atlantic transect. Deep Sea Res. Part II 116, 283–302.
Pavia, F., Anderson, R., Vivancos, S., Fleisher, M., Lam, P., Lu, Y., Edwards, R.L., 2018. Intense hydrothermal scavenging of 230Th and 231Pa in the deep Southeast Pacific. Mar. Chem. 201, 212–228.
Pavia, F.J., Anderson, R.F., Black, E.E., Kipp, L.E., Vivancos, S.M., Fleisher, M.Q., Edwards, R.L., 2019. Timescales of hydrothermal scavenging in the South Pacific Ocean from ^{234}Th, ^{230}Th, and ^{228}Th. Earth Planet. Sci. Lett. 506, 146–156.
Pavia, F.J., Anderson, R.F., Pinedo-Gonzalez, P., Fleisher, M.Q., Brzezinski, M.A., Robinson, R.S., 2020. Isopycnal transport and scavenging of ^{230}Th and ^{231}Pa in the Pacific Southern Ocean. Global Biogeochem. Cycles 34 (12), e2020GB006760.
Pöppelmeier, F., Jeltsch-Thömmes, A., Lippold, J., Joos, F., Stocker, T.F., 2023. Multi-proxy constraints on Atlantic circulation dynamics since the last ice age. Nat. Geosci. 16 (4), 349–356.
Redmond, N.A., Hayes, C.T., Anderson, R.F., Black, E.E., Edwards, R.L., Fleisher, M.Q., Mateos, K.C., 2025. Hydrothermal plumes act as a regional boundary sink of 230Th in the Equatorial Pacific. Global Biogeochem. Cycles 39 (4), e2024GB008219.
Rempfer, J., Stocker, T.F., Joos, F., Lippold, J., Jaccard, S.L., 2017. New insights into cycling of ^{231}Pa and ^{230}Th in the Atlantic Ocean. Earth Planet. Sci. Lett. 468, 27–37.
Resing, J.A., Sedwick, P.N., German, C.R., Jenkins, W.J., Moffett, J.W., Sohst, B.M., Tagliabue, A., 2015. Basin-scale transport of hydrothermal dissolved metals across the South Pacific Ocean. Nature 523 (7559), 200–203.
Rixen, T., Gaye, B., Emeis, K.C., Ramaswamy, V., 2019. The ballast effect of lithogenic matter and its influences on the carbon fluxes in the Indian Ocean. Biogeosciences 16 (2), 485–503.
Robert, J., Miranda, C.F., Muxart, R., 1969. Mesure de la période du protactinium 231 par microcalorimétrie. Radiochim. Acta 11 (2), 104–108.
Roshan, S., DeVries, T., Wu, J., John, S., Weber, T., 2020. Reversible scavenging traps hydrothermal iron in the deep ocean. Earth Planet. Sci. Lett. 542, 116297.
Sasaki, Y., Kobayashi, H., Oka, A., 2022. Global simulation of dissolved ^{231}Pa and ^{230}Th in the ocean and the sedimentary ^{231}Pa/^{230}Th ratios with the ocean general circulation model COCO ver4. 0. Geosci. Model Dev. 15 (5), 2013–2033.

Scheen, J., Lippold, J., Pöppelmeier, F., Süfke, F., Stocker, T.F., 2025. Promising regions for detecting the overturning circulation in Atlantic $^{231}Pa/^{230}Th$: a model-data comparison. Paleoceanogr. Paleoclimatol. 40 (3), e2024PA004869.
Tagliabue, A., Bopp, L., Dutay, J.C., Bowie, A.R., Chever, F., Jean-Baptiste, P., Jeandel, C., 2010. Hydrothermal contribution to the oceanic dissolved iron inventory. Nat. Geosci. 3 (4), 252–256.
Tagliabue, A., Aumont, O., DeAth, R., Dunne, J.P., Dutkiewicz, S., Galbraith, E., Yool, A., 2016. How well do global ocean biogeochemistry models simulate dissolved iron distributions? Global Biogeochem. Cycles 30 (2), 149–174.
Tagliabue, A., Bowie, A.R., Boyd, P.W., Buck, K.N., Johnson, K.S., Saito, M.A., 2017. The integral role of iron in ocean biogeochemistry. Nature 543 (7643), 51–59.
Tagliabue, A., Bowie, A.R., DeVries, T., Ellwood, M.J., Landing, W.M., Milne, A., Boyd, P. W., 2019. The interplay between regeneration and scavenging fluxes drives ocean iron cycling. Nat. Commun. 10 (1), 4960.
Tagliabue, A., Buck, K.N., Sofen, L.E., Twining, B.S., Aumont, O., Boyd, P.W., Sedwick, P., 2023. Authigenic mineral phases as a driver of the upper-ocean iron cycle. Nature 620 (7972), 104–109.
Teng, Y.C., Primeau, F.W., Moore, J.K., Lomas, M.W., Martiny, A.C., 2014. Global-scale variations of the ratios of carbon to phosphorus in exported marine organic matter. Nat. Geosci. 7 (12), 895–898.
Wang, W.L., Fu, W., Le Moigne, F.A., Letscher, R.T., Liu, Y., Tang, J.M., Primeau, F.W., 2023. Biological carbon pump estimate based on multidecadal hydrographic data. Nature 624 (7992), 579–585.
Wang, W.L., Moore, J.K., Martiny, A.C., Primeau, F.W., 2019. Convergent estimates of marine nitrogen fixation. Nature 566 (7743), 205–211.
Weber, T., John, S., Tagliabue, A., DeVries, T., 2018. Biological uptake and reversible scavenging of zinc in the global ocean. Science 361 (6397), 72–76.
Xu, H., Weber, T., 2025. Quantifying lithogenic inputs to the ocean from the GEOTRACES thorium transects in a data-assimilation model. Global Biogeochem. Cycles 39 (6), e2024GB008485.